

Stability of Perovskite Films Encapsulated in Single- and Multi-Layer Graphene Barriers

Rory Runser,[†] Moses Kodur,[†] Justin H. Skaggs, Deniz N. Cakan, Juliana B. Foley, Mickey Finn III, David P. Fenning,* and Darren J. Lipomi*



Cite This: <https://doi.org/10.1021/acsaem.1c02240>



Read Online

ACCESS |



Metrics & More



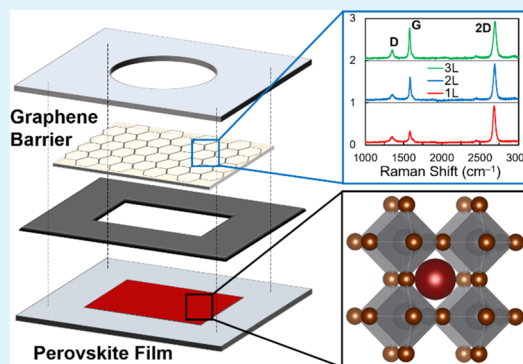
Article Recommendations



Supporting Information

ABSTRACT: This paper describes the efficacy of barrier films coated with single- and multi-layer graphene in preventing degradation of perovskite films in air. Despite the impermeability of graphene to small species such as water and oxygen, the presence of numerous grain boundaries and defects in chemical vapor deposition (CVD)-grown graphene monolayer films can present pathways for permeation. However, the availability of these pathways can in principle be reduced by stacking multiple layers of graphene on top of each other. The barrier material considered here consists of the semi-permeable polymer parylene laminated with either 0, 1, 2, or 3 monolayers of graphene. These composite films are used to encapsulate triple cation perovskite films, which are then subjected to a degradation test under damp heat. We find that a monolayer of graphene confers a 15-fold reduction in degradation compared to the parylene films with no graphene and that three-layer graphene can yield a further 2× reduction in degradation. Although all of our films encapsulated with graphene/parylene exhibited substantial degradation compared to films encapsulated in glass with polyisobutylene edge seals, our results nonetheless reinforce the utility of graphene barriers for less demanding applications, including lightweight or flexible perovskite solar cells with shorter anticipated lifetimes.

KEYWORDS: perovskites, multi-layer graphene, photovoltaics, accelerated testing, encapsulation



1. INTRODUCTION

The stability of perovskite solar cells (PSCs) remains one of the major challenges on the path of their commercialization and deployment.¹ While the record efficiencies of PSCs continue to rise,^{2,3} their sensitivity to environmental factors such as moisture,^{4,5} oxygen,⁶ temperature,⁷ and light^{8,9} limit their economic and practical viability. To address these concerns, researchers have undertaken several lines of inquiry to extend the lifetimes of PSCs. These areas of research focus fall broadly into three categories: (1) the development of new perovskite compositions with greater intrinsic stability (e.g., mixed cation and/or halides);^{10–13} (2) the optimization of interfaces within devices, so as to minimize defects and vacancies;^{4,6,14,15} and (3) the encapsulation of devices to slow the ingress of moisture and oxygen.^{16–20} Our work here focuses predominantly on the third of these research thrusts.

To measure the stability against these stressors, researchers often use accelerated degradation studies in which materials or whole devices are subjected to extreme conditions that simulate long-term degradation. Recently, the research community has attempted to standardize testing protocols to aid in the comparison of stability measured in different laboratories.²¹ For example, the vulnerability of perovskites to heat, moisture, and oxygen can be simultaneously evaluated

using “damp heat testing,” in which devices or films are subjected to high temperatures and humidity to rapidly simulate the effects of long-term degradation.^{4–6,22,23} These accelerated testing conditions have proven to be a challenging stability threshold for perovskite photovoltaics to overcome due to their intrinsic sensitivity to oxygen and water.^{5,16,24–26} One obstacle in devising scalable encapsulation schemes for PSC is that typical materials used for encapsulation of solar cells or other semiconductors—typically ethylene vinyl acetate or other polyolefins—require processing temperatures often ~150 °C.^{27,28} In PSCs, however, such temperatures can destabilize the perovskite absorber, the hole-transport layer (HTL), or both.^{29,30} As a result, PSCs often exhibit a reduction in efficiency after encapsulation,²³ and relatively long-lasting PSCs have a lower efficiency compared to record devices.³¹ It is therefore critical to investigate new barrier materials and encapsulation techniques that are compatible with PSCs.

Received: July 28, 2021



ACS Publications

© XXXX American Chemical Society

A

<https://doi.org/10.1021/acsaem.1c02240>
ACS Appl. Energy Mater. XXXX, XXX, XXX–XXX

Graphene is an intriguing material for thin-film, flexible barriers due to the impermeability of its basal plane to gases³² as well as its high optical transmissivity.³³ In this paper, we investigate the efficacy of the graphene barriers toward preventing the degradation of perovskite films, using an encapsulation scheme as shown in Figure 1. The use of a low-

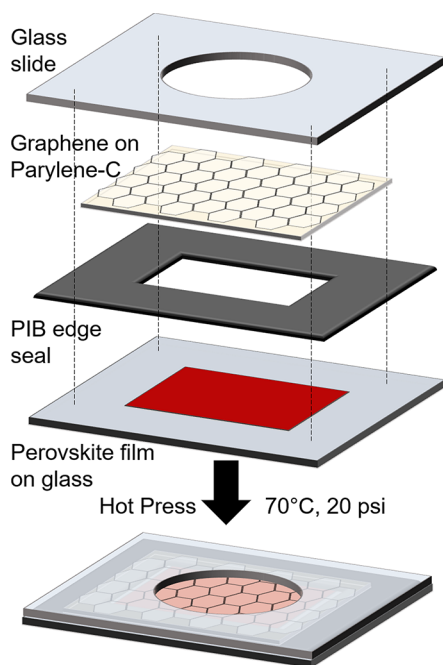


Figure 1. Schematic drawing of the encapsulation process.

temperature-activating polyisobutylene (PIB) edge seal results in a high-quality encapsulation without causing degradation of the film and ensures that any small species ingress is through the barrier film being investigated.^{16,34,35} Numerous papers already speculate an enhancement to the stability of perovskite solar cells (PSCs) when encapsulated with graphene.^{4,36} Graphene derivatives, including fluorine-doped nanoplatelets³⁷ and graphene oxides,^{38,39} have also been shown to increase the stability of PSCs. Various studies have also incorporated graphene into PSCs as an electrode material (due to the electrical conductivity of graphene) either in combination with or separate from barrier applications.^{40,41} Nonetheless, the presence of grain boundaries and defects within chemical vapor

deposition (CVD) graphene can provide numerous permeation pathways for species such as water and oxygen.⁴² As a result, many reports of improved PSC stability due to encapsulation with graphene may not be due entirely to graphene itself but rather aided by the polymeric support layer on which the graphene has adhered.

One method to reduce the availabilities of these pathways for the permeation of gases is by stacking multiple monolayers of graphene. With multiple layers, transport through grain boundaries and pinholes may become blocked by adjoining layers.⁴³ Here, we measure the performance of the barriers composed of up to three layers of graphene (Figure 2a), beyond which the cost, complexity of fabrication, and optical losses (2.3% per layer of graphene)³³ (Figure 2b) would be impractical for optoelectronic devices, such as thin-film solar cells.

2. MATERIALS AND METHODS

2.1. Materials. Formamidinium iodide (FAI) and methylammonium bromide (MABr) were purchased from Greatcell Solar Materials. CsI (99.999% purity), dimethylsulfoxide (DMSO) (99.9% purity), dimethylformamide (DMF) (99.9% purity), and chlorobenzene (99.9% purity) were purchased from Sigma-Aldrich. PbI_2 (99.99% purity) and PbBr_2 (99.99% purity) were purchased from TCI. Poly(methyl methacrylate) (PMMA, $M_w = 550\,000$) was obtained from Alfa Aesar. Ammonium persulfate (APS) and anisole were obtained from Acros Organics. Prior to use, all solvents were dried for 24 h with 3 Å molecular sieves (VWR, grade 564, mesh 8–12) and then filtered with a 0.22 μm poly(tetrafluoroethylene) (PTFE) syringe filter. Monolayer CVD graphene on copper foil and monolayer graphene mounted on 10 μm parylene-C were supplied by Grolltex, Inc, with a >95% surface coverage of graphene as determined by optical microscopy. Polyisobutylene (PIB) edge seal sheets were obtained from Quanex.

2.2. Preparation of Graphene Barriers. Monolayer graphene on 10 μm parylene-C (hereafter referred to as 1L) was used as is. The procedure we used to prepare two-layer (2L) and three-layer (3L) graphene on parylene-C involves iterative deposition of monolayer graphene,^{44,45} as shown in Figure 2a. Briefly, monolayer graphene on copper foil (5 cm \times 5 cm) was spin-coated with a 4 wt % PMMA solution in anisole at 4000 rpm for 60 s. After annealing at 150 $^\circ\text{C}$ for 5 min to remove any remaining anisole, the copper was etched in a 0.05 g/mL solution of APS in water for 2 h, until fully dissolved. The resulting floating PMMA/graphene was transferred to a clean water bath. Separately, a 5 cm \times 5 cm piece of 1L graphene was taped to a glass slide, graphene facing up. The PMMA/graphene was transferred directly onto the 1L film, with the two graphene layers in direct contact, and allowed to dry overnight in a desiccator. Finally, the

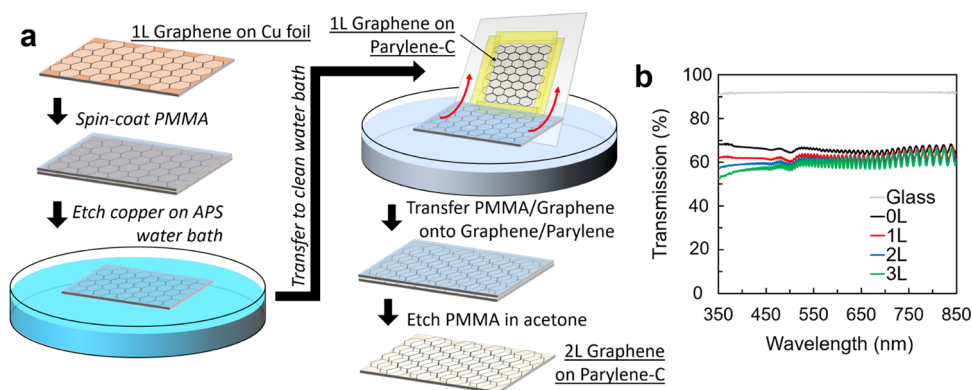


Figure 2. Preparation of multi-layer graphene barrier films. (a) Schematic illustration of the fabrication of 2-layer graphene on parylene. (b) UV-vis transmission spectra of graphene-on-parylene barriers as a function of the number of graphene layers.

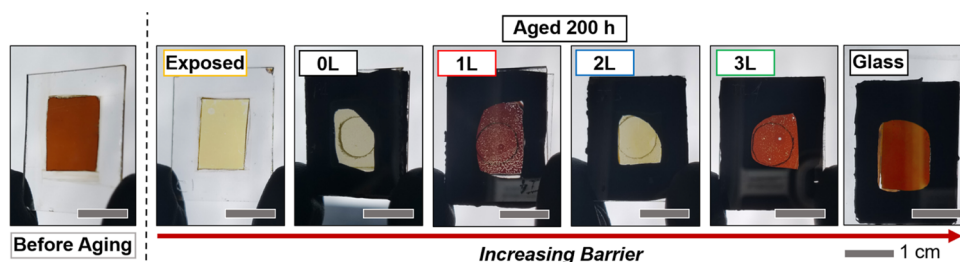


Figure 3. Pictures of representative films before and after aging for 200 h.

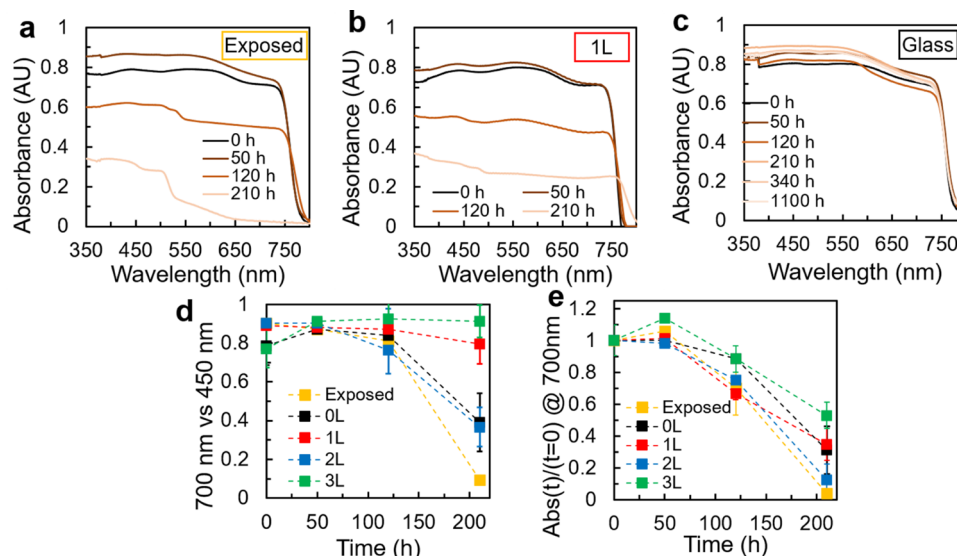


Figure 4. UV-vis tracking during perovskite film aging. (a–c) Evolution of UV-vis spectra for (a) exposed, (b) 1L, and (c) glass-encapsulated films. The remaining UV-vis spectra are given in Figure S1. (d) Ratio of absorbance intensity at 700 vs 450 nm. (e) Ratio of absorbance intensity at 700 nm at t vs $t = 0$.

PMMA was removed by etching in a 50 °C bath of acetone for 5 min, then rinsed with IPA and allowed to dry. This process was repeated once more to yield 3-layer graphene. Successful graphene transfer was confirmed via UV-vis (Figure 2b), showing a successive decrease in optical transmission with each layer of graphene added. Lastly, 0L graphene (aka plain 10 μ m parylene-C) was obtained by treating 1L films with plasma (30 W) for 30 s at a base pressure of 250 mTorr of air. Graphene removal was confirmed via sheet resistance measurements, which showed no conductivity in the resulting films, as well as UV-vis showing an increase in optical transmission (Figure 2b).

2.3. Preparation of Perovskite Films. Substrates—glass or fluorine-doped tin oxide (FTO)—were cleaned through a series of sonication (15 min) and rinse steps in the following sequence: 2 v% Hellmanex in deionized (DI) water, DI water, isopropanol, and acetone. Afterward, the substrates were rinsed in IPA and dried with compressed air.

The triple cation perovskite films were prepared in a nitrogen-filled glovebox. First, two separate solutions of 1.5 M lead iodide and 1.5 M lead bromide were prepared with a 9:1 volume ratio of DMF and DMSO used as a solvent. The solutions were vortexed and then heated to 100 °C for 10 min. The PbI_2 solution was added to FAI, and PbBr_2 solution was added to MABr such that 1.22 M solutions of FAPbI_3 and MAPbBr_3 , respectively, with a 1.09 over-stoichiometric ratio of the lead salts were formed (using the 9:1 DMF/DMSO solution to dilute as necessary). An additional solution of 1.5 M CsI in DMSO was prepared in the glovebox and heated at 150 °C for 10 min. The FAPbI_3 and MAPbBr_3 solutions were mixed together in a 5:1 ratio and 5% molar ratio (with respect to the A-site) of CsI was added to the final solution, resulting in a nominal stoichiometry of $\text{FA}_{0.79}\text{MA}_{0.16}\text{Cs}_{0.05}\text{Pb}(\text{I}_{0.84}\text{Br}_{0.16})_3$.

The perovskite films were formed by spin-coating. Prior to deposition, the substrates were treated with air-based plasma for 10 min at 300 mTorr. Briefly, 90 μ L of the solution was dropped onto the substrate and doctor-bladed across the entire surface. The first step of the spin-cast at 1000 RPM for 10 s served to remove excess solution and ensure an even spread across the entirety of the substrate. In the second step, the speed was increased to 5500 RPM for 20 s. Then, 250 μ L of chlorobenzene was dispensed rapidly (in approximately 1 s) after 8 s had expired in step 2 of the spin-coat. The films were annealed on a hot plate for 45 min at 100 °C, resulting in a final thickness of 550 nm.

2.4. Encapsulation of Films. The assembly of the encapsulated films is shown in Figure 1. After spin-coating of the perovskite films, the edges of the film (approximately 0.5 cm) were wiped away with methoxyethanol and a cotton swab. PIB edge seal sheets were cut into 2.5 cm \times 2 cm rectangles from which a 2 cm \times 1.5 cm rectangle was cut out from the center. Barrier films were cut to 2.25 cm \times 1.75 cm rectangles and placed onto glass slides, which had a 1 cm hole drilled out from the center. Adhesive PIB edge seal pieces were then placed on top and pressed with tweezers to hold in place. These barrier/glass slides were then transferred to the glovebox, where perovskite films were pressed onto the PIB edge seal. The films were then placed onto a hot plate at 70 °C, under a mass exerting a pressure of 20 psi to activate the edge seal. After 20 min, the samples were removed from the hot plate and allowed to cool. For the samples encapsulated in glass, a 2.5 cm \times 2 cm glass slide was stuck with PIB edge seal directly onto the perovskite film. Additional control (exposed) samples with no barrier were also prepared.

2.5. Film Monitoring. The samples were placed into a humidity chamber at 65 °C, 85% relative humidity (ISOS-D-3 testing protocol).²¹ The films were removed from the humidity chamber at

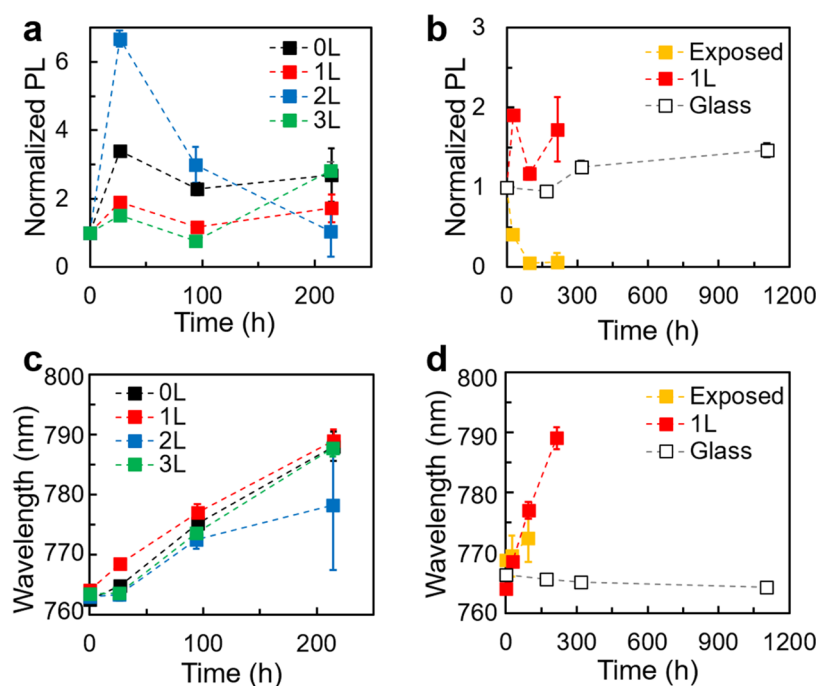


Figure 5. Photoluminescence (PL) evolution during aging. (a) Normalized average PL evolution for 0, 1, 2, and 3L graphene. (b) PL evolution comparing 1L to glass and control samples. (c) Peak PL wavelength evolution for 0, 1, 2, and 3L graphene. (d) Evolution of peak PL wavelength comparing 1L to glass and exposed samples.

regular intervals and analyzed via photoluminescence (PL) measurements and UV–vis spectroscopy. Photoluminescence measurements were taken using a Renishaw Raman/microPL microscope with a 633 nm excitation laser, 600 mm^{−1} grating. UV–vis measurements were taken on a Perkin Elmer LAMBDA 1050+ UV/Vis/NIR spectrophotometer. For each condition, five films were prepared and aged while two films were actively monitored. At the end of the aging test, the encapsulation was removed from the films to enable analysis via X-ray diffraction (XRD). XRD measurements were taken using a Rigaku SmartLab diffractometer. Pictures of the films before and after aging for 200 h are shown in Figure 3.

3. RESULTS AND DISCUSSION

The optical absorbance evolution of select perovskite films is shown in Figures 4a–c and S1. As seen in Figure 4a, the exposed films quickly tended toward optical transparency, retaining only a small amount of absorbance at shorter (purple) wavelengths (and thus appearing light yellow—see Figure 3). This trend is attributed to the degradation to and subsequent outgassing of volatile species (such as methylammonium iodide and HI) from the perovskite film.⁴⁶ Figure 4b shows the UV–vis evolution for the 1L-encapsulated films, where the decrease in absorbance was also observed but was less rapid. The 0L, 2L, and 3L graphene/parylene samples showed similar behavior (Figure S1b–e). Finally, the glass-encapsulated films (Figure 4c) showed minimal variation in absorbance during aging, confirming the quality of the PIB edge seal as well as the strong thermal stability of the perovskite (the glass-encapsulated samples were left to age an additional 800 h after the remaining samples were removed from the humidity chamber and still displayed minimal signs of degradation). We observed distinct absorbance profiles between the exposed/0L/2L samples and the 1L/3L samples. The former set showed a marked decrease in absorbance at longer wavelengths, which we attribute to the conversion of perovskite into PbI₂, which is optically absorbent only below

550 nm.⁴⁷ The latter set, in contrast, continued to absorb light up to 750 nm throughout the aging test due to the continued presence of perovskite. These observations are clarified by considering absorbance at 450 nm (where absorbance from the triple cation perovskite, δ -FAPbI₃,⁴⁸ and PbI₂ are observed) and at 700 nm (which is only absorbed by the perovskite). In Figure 4d, the ratio of absorbance between 450 and 700 nm is shown as a function of time. Here, the 1L/3L samples retained ~2× more absorbance at longer wavelengths than the 0L/2L samples, which themselves were ~3× more absorbent than the exposed film. Additionally, when the time evolution of absorbance at 700 nm is considered (Figure 4e), we observe that 3L retains much more perovskite relative to the other barrier films. However, a significant loss is still realized even in the 3L condition. Figure 3, showing photos of the aged film, also mirrors this trend, with the exposed/0L/2L films appearing yellow, compared to the red-colored 1L/3L films (though visually, some spottiness is apparent in the 1L/3L films, indicative of degradation in those films as well). The 2L graphene exhibits worse performance than the 1L due to the handling required to coat the additional graphene layer onto the commercial 1L graphene/parylene (see Figure 2), which can induce defects/tears in graphene.⁴⁹ The decrease of performance upon the addition of a second graphene layer was observed across all five films that were aged. Additionally, multiple sets of 2L films prepared from different batches of graphene exhibited diminished performance, as confirmed by conductivity and Raman measurements.

To complement the information gained from tracking optical absorbance, we also monitored the films' photoluminescence (PL) behavior over time, which can give insight into the films' optoelectronic properties. These results are shown in Figures S2 and 5. To improve readability, the evolution of the peak PL intensity (Figure 5a,b) and peak PL wavelength (Figure 5c,d) have each been split into 2 panels,

with the same data from the 1L-encapsulated sample represented in both panels. As shown in Figure 5a, all of the graphene/parylene films exhibit an increase in PL over time, despite becoming yellow/spotty during aging (Figure 3). In early trials, we considered that this phenomenon could be due to condensation forming on the graphene/parylene barrier, potentially amplifying the PL emissions back to the detector. Thus, in later trials, we carefully dried the exposed barrier films with an air gun prior to every PL measurement, and this phenomenon persisted. In contrast, the exposed films exhibited no photoluminescence under laser excitation by 100 h, while the glass-encapsulated films showed only a slight increase in PL emission. (Figure 5b). In addition, the graphene/parylene-encapsulated samples exhibited a shift in the peak wavelength of PL emissions (Figure 5c), a behavior not present in the glass films and only minimally observed in exposed films (Figure 5d).

Further understanding of the differences in perovskite decay was achieved via probing the crystallographic properties of the films through X-ray diffraction (XRD). The X-ray diffractograms for our films before and after aging for 200 h are shown in Figure 6a (and re-plotted in Figure S3 to show the full peak

formed only in the presence of the semi-permeable parylene encapsulation material.

The X-ray diffractograms also allow for qualitative estimation of the relative degree of conversion between triple cation perovskite and δ -FAPbI₃ between the graphene/parylene films by comparing the intensities of the peaks at 14 and 11.5°. This ratio is plotted in Figure 6b and shows the dramatic effect that the addition of graphene conveys to the parylene support layer. While the triple cation perovskite in the 0L graphene has almost completely decayed into δ -FAPbI₃, the 1L graphene film has a 15× higher ratio of triple cation to δ -FAPbI₃, which itself is nearly doubled again between the 1L and 3L graphene. Meanwhile, the 2L films exhibited worse performance than either the 1L or 3L films, a similar trend as seen via optical absorbance and PL emission. The addition of a 3rd layer of graphene (3L) appears able to negate and improve upon any damaging wrinkles/tears induced by the multi-layer graphene preparation.

These observations suggest that our set of films have undergone three unique degradation pathways. The first, seen in the exposed films, is the degradation of the triple cation perovskite into PbI₂,⁵⁰ along with the expulsion of all volatile species. The second, observed in the glass-encapsulated samples, is a slow thermal anneal due to the elevated temperature (85 °C) of the humidity chamber used for the accelerated decay test. The effect is a reduction of non-radiative recombination centers (leading to a slight PL increase) without changes to the chemical composition of the films, as there is no pathway for species ingress/egress. The final degradation pathway observed, seen in the graphene/parylene films, is the phase segregation and formation of multiple perovskite phases, particularly iodide-rich and bromide-rich domains. This is exhibited by the increased and red-shifted PL profile, which is attributed to the iodine-rich phases acting as a carrier sink.⁵¹ Additionally, photoinactive phases (such as δ -FAPbI₃ and potentially I₂⁵⁰) are forming due to the ingress of oxygen and water.⁵²

A more detailed analysis of the graphene barriers, separate from the perovskite films, was carried out to validate our findings. Figure 7a shows the sheet resistance of the graphene films. The increasing conductivity as each layer is added, as well as the overall magnitude of sheet resistance, are consistent with the previous reports.⁴⁴ The average optical transmissivity of the films (Figure 7b) likewise shows a successive change with each layer added, further confirming the successful transfer. In contrast, air permeability measurements (Figure 7c) show a large (15×) decrease between 0L and 1L, followed by smaller variations from 1L to 2L to 3L. Notably, the difference between the permeability of 0L vs 1L films is identical to the difference in the ratio of the triple cation perovskite/ δ -FAPbI₃ shown in Figure 6b. Meanwhile, the minimal variations in air permeability between the single- and multi-layer graphene barriers are in sharp contrast to the varied perovskite degradation observed, with 2L films decaying substantially compared to 1L and 3L films.

To investigate this discrepancy, spatial mapping using Raman was conducted to analyze the quality of the graphene films and spatial resolution. We note that Raman analysis cannot be done directly onto the parylene films, whose spectra overwhelm the graphene signal and must instead be measured following water transfer onto a silicon substrate. The overlain spectra for 30 measurements for 1L graphene, given in Figure S7a–c shows a wide range of graphene quality, and numerous

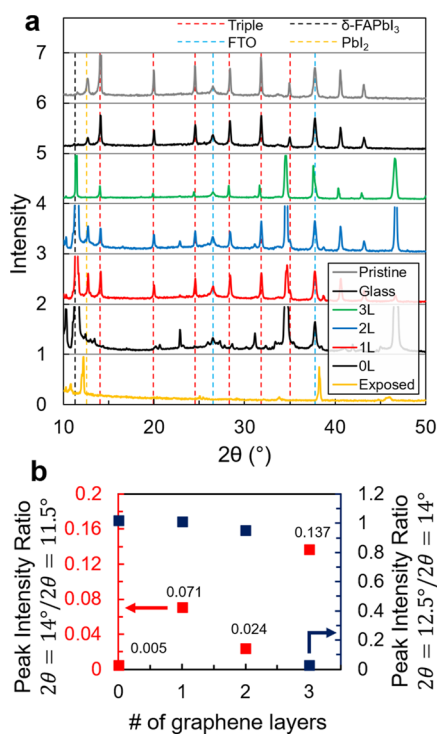


Figure 6. XRD analysis of perovskite films. (a) XRD diffractograms for films before and after aging. (b) Ratio of peak intensity of triple cation perovskite ($2\theta = 14^\circ$) to peak intensity of δ -FAPbI₃ ($2\theta = 11.5^\circ$) and PbI₂ peak intensity ($2\theta = 12.5^\circ$) as a function of the number of layers of graphene.

heights). The glass-encapsulated films remained virtually unchanged compared to films analyzed before aging, in alignment with the trends observed with UV–vis and PL. In contrast, the graphene/parylene films all exhibited a substantial decrease in intensity of the triple cation perovskite peak at $2\theta = 14^\circ$ while also gaining a prominent peak at $2\theta = 11.5^\circ$, corresponding to the hexagonal δ -FAPbI₃. The δ -FAPbI₃ peak is not seen in either the exposed or glass-encapsulated films; it

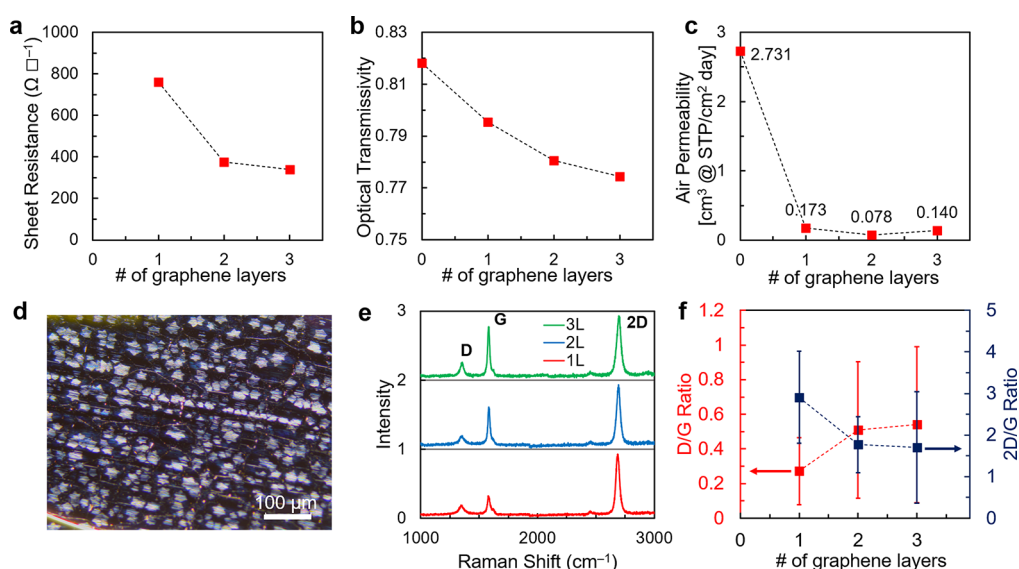


Figure 7. Analysis of single- and multi-layer graphene barrier films. (a) Sheet resistance of films as a function of the number of layers (0L films produced an open circuit). (b) Average optical transmissivity (extracted from Figure 1b). (c) Air permeability of films found using an isochoric gas permeability apparatus (see Figures S4, S5, Tables S1 and S2 for detailed procedure and calculations). (d) Optical micrograph of 1L graphene, as received. (e) Representative Raman spectra of 1L, 2L, and 3L graphene films (for spatial mapping of graphene, see Figure S6). (f) Average D/G and 2D/G ratio for graphene films.

traces show minimal or no graphene signal. Indeed, the spatial coverage of transferred graphene was less than 50% for both 1L and 2L films, coupled with large variability in the 2D/G ratio (Figures 6 and S7d), which gives information regarding the number of monolayers of graphene.⁵³ Several factors likely influence the lack of uniformity and variability in coverage of the graphene films. First, nanoislands and macroscopic regions of multi-layer graphene are commonly found on CVD-grown graphene (see Figure 7d) and are formed via nucleation from silica or other impurities within the copper foil on which it is grown;^{54,55} thus, a uniform monolayer of graphene is unlikely to be present in the 1L films to begin with. Additionally, the water transfer method for layer-by-layer growth of multi-layer graphene is easily susceptible to wrinkling and tearing.⁴⁹ Although a previous work by Yoon, et al. on multi-layer graphene films (prepared via the same method as our own films) claims that that strong van der Waals forces between graphene layers can fully suppress lateral diffusion of air molecules,⁵⁶ the authors note that in cracked regions, air molecules will indeed diffuse laterally, allowing them to access adjoining grain boundaries and pinholes and permeate vertically through the film. We note that a graphene grain boundary typically refers to a tilt grain boundary comprised of 5- and 7-membered rings,^{57,58} through which small species are able to permeate.⁵⁹ The wide variability in graphene uniformity and coverage in our multi-layer (i.e., 2L and 3L) films will therefore result in highly variable barrier properties over a large (~cm²) area. Given the penalties of increased process complexity and materials cost of each successive layer of graphene used, compared to the small improvement in perovskite film stability shown between 1L and 3L graphene, we conclude that 1L graphene may offer the best combination of properties for use in flexible, optically transparent barrier applications for perovskite films. Beyond single- and multi-layer graphene, other 2D materials may prove to be intriguing for similar encapsulation applications. As an example, graphene oxide also exhibits a good barrier performance against air and

water,⁶⁰ although thickness would need to be carefully controlled to retain optical transmissibility.⁶¹ Meanwhile, hexagonal boron nitride has recently emerged as a promising new 2D material and exhibits excellent transparency due to its wide bandgap,⁶² although it tends to have smaller grains than CVD graphene,⁶³ which could exacerbate the leakage issues we observed.

4. CONCLUSIONS

Experimental results show that single-layer graphene can confer substantially improved barrier performance to a polymeric support film, with multi-layer (at least 3L) graphene yielding further improved barrier performance. We emphasize that 2L graphene exhibited worse performance as an encapsulant than 1L graphene, most likely due to defects introduced during the manipulation of the films. Nevertheless, all of our graphene/parylene-encapsulated films showed substantial degradation compared to glass-encapsulated films, suggesting that for rigid, non-flexible, long-lasting applications, the addition of graphene to a semi-permeable flexible polymer barrier is insufficient for generating a highly stable device. While modifications to the preparation procedure of the multi-layer graphene could result in improved barrier performance, the numerous grain boundaries in CVD graphene still result in a bulk material that is far from attaining the “impermeable” status of glass or molecular graphene. Still, the substantial improvement obtained from the addition of a single layer of graphene to our polymer support layer makes graphene-based barriers a compelling potential encapsulant for lightweight and/or flexible perovskite solar cells.

■ ASSOCIATED CONTENT

Supporting Information

The Supporting Information is available free of charge at <https://pubs.acs.org/doi/10.1021/acsaem.1c02240>.

UV–vis evolution, photoluminescence evolution, and X-ray diffractograms of perovskite films; pictures of

isochoric gas permeability apparatus with calculations for gas permeability values (tabulated); and Raman spectra of graphene barrier films (PDF)

AUTHOR INFORMATION

Corresponding Authors

David P. Fenning – Department of NanoEngineering, University of California, San Diego, La Jolla, California 92093-0448, United States; orcid.org/0000-0002-4609-9312; Email: dfenning@eng.ucsd.edu

Darren J. Lipomi – Department of NanoEngineering, University of California, San Diego, La Jolla, California 92093-0448, United States; orcid.org/0000-0002-5808-7765; Email: dlipomi@eng.ucsd.edu

Authors

Rory Runser – Department of NanoEngineering, University of California, San Diego, La Jolla, California 92093-0448, United States

Moses Kodur – Department of NanoEngineering, University of California, San Diego, La Jolla, California 92093-0448, United States; orcid.org/0000-0002-3890-2945

Justin H. Skaggs – Department of NanoEngineering, University of California, San Diego, La Jolla, California 92093-0448, United States

Deniz N. Cakan – Department of NanoEngineering, University of California, San Diego, La Jolla, California 92093-0448, United States

Juliana B. Foley – Department of NanoEngineering, University of California, San Diego, La Jolla, California 92093-0448, United States

Mickey Finn III – Department of NanoEngineering, University of California, San Diego, La Jolla, California 92093-0448, United States

Complete contact information is available at: <https://pubs.acs.org/10.1021/acsaem.1c02240>

Author Contributions

[†]R.R. and M.K. contributed equally to this work.

Notes

The authors declare no competing financial interest.

ACKNOWLEDGMENTS

This work was supported by the California Energy Commission (CEC) Grant Number EPC-16-050. R.R. also received support from the National Science Foundation Graduate Research Fellowship under Grant no. DGE-1144086. The authors also thank Yuan Zeng and the Nanoscale Interfaces Assembly Lab at UCSD for the technical support of PL measurements, Hayley Hirsh for helpful discussions on XRD analysis, Yanqi Luo for advice regarding perovskite synthesis, and Alex Zaretski for assistance with graphene transfer methods and air permeability measurements. The authors acknowledge the use of facilities and instrumentation supported by the National Science Foundation through the University of California San Diego Materials Research Science and Engineering Center DMR-2011924.

REFERENCES

- (1) Rao, M. K.; Sangeetha, D. N.; Selvakumar, M.; Sudhakar, Y. N.; Mahesha, M. G. Review on Persistent Challenges of Perovskite Solar Cells' Stability. *Sol. Energy* **2021**, *218*, 469–491.
- (2) Jeong, J.; Kim, M.; Seo, J.; Lu, H.; Ahlawat, P.; Mishra, A.; Yang, Y.; Hope, M. A.; Eickemeyer, F. T.; Kim, M.; Yoon, Y. J.; Choi, I. W.; Darwich, B. P.; Choi, S. J.; Jo, Y.; Lee, J. H.; Walker, B.; Zakeeruddin, S. M.; Emsley, L.; Rothlisberger, U.; Hagfeldt, A.; Kim, D. S.; Grätzel, M.; Kim, J. Y. Pseudo-Halide Anion Engineering for α -FAPbI₃ Perovskite Solar Cells. *Nature* **2021**, *592*, 381–385.
- (3) Green, M. A.; Dunlop, E. D.; Hohl-Ebinger, J.; Yoshita, M.; Kopidakis, N.; Ho-Baillie, A. W. Y. Solar Cell Efficiency Tables (Version 55). *Prog. Photovoltaics* **2020**, *28*, 3–15.
- (4) Hu, X.; Jiang, H.; Li, J.; Ma, J.; Yang, D.; Liu, Z.; Gao, F.; Liu, S. Air and Thermally Stable Perovskite Solar Cells with CVD-Graphene as the Blocking Layer. *Nanoscale* **2017**, *9*, 8274–8280.
- (5) Song, Z.; Abate, A.; Wathage, S. C.; Liyanage, G. K.; Phillips, A. B.; Steiner, U.; Graetzel, M.; Heben, M. J. Perovskite Solar Cell Stability in Humid Air: Partially Reversible Phase Transitions in the PbI₂-CH₃NH₃I-H₂O System. *Adv. Energy Mater.* **2016**, *6*, No. 1600846.
- (6) Habisreutinger, S. N.; Leijtens, T.; Eperon, G. E.; Stranks, S. D.; Nicholas, R. J.; Snaith, H. J. Carbon Nanotube/Polymer Composites as a Highly Stable Hole Collection Layer in Perovskite Solar Cells. *Nano Lett.* **2014**, *14*, 5561–5568.
- (7) Akbulatov, A. F.; Luchkin, S. Y.; Frolova, L. A.; Dremova, N. N.; Gerasimov, K. L.; Zhidkov, I. S.; Anokhin, D. V.; Kurmaev, E. Z.; Stevenson, K. J.; Troshin, P. A. Probing the Intrinsic Thermal and Photochemical Stability of Hybrid and Inorganic Lead Halide Perovskites. *J. Phys. Chem. Lett.* **2017**, *8*, 1211–1218.
- (8) Tan, W.; Bowring, A. R.; Meng, A. C.; McGehee, M. D.; McIntyre, P. C. Thermal Stability of Mixed Cation Metal Halide Perovskites in Air. *ACS Appl. Mater. Interfaces* **2018**, *10*, 5485–5491.
- (9) Kanda, H.; Usiobo, O. J.; Momblona, C.; Abuhelaiaq, M.; Sutanto, A. A.; Igci, C.; Gao, X. X.; Audinot, J. N.; Wirtz, T.; Nazeeruddin, M. K. Light Stability Enhancement of Perovskite Solar Cells Using 1H,1H,2H,2H-Perfluorooctyltriethoxysilane Passivation. *Sol. RRL* **2021**, *5*, No. 2000650.
- (10) Ono, L. K.; Juarez-Perez, E. J.; Qi, Y. Progress on Perovskite Materials and Solar Cells with Mixed Cations and Halide Anions. *ACS Appl. Mater. Interfaces* **2017**, *9*, 30197–30246.
- (11) Cai, Y.; Wang, S.; Sun, M.; Li, X.; Xiao, Y. Mixed Cations and Mixed Halide Perovskite Solar Cell with Lead Thiocyanate Additive for High Efficiency and Long-Term Moisture Stability. *Org. Electron.* **2018**, *53*, 249–255.
- (12) Saliba, M.; Matsui, T.; Domanski, K.; Seo, J. Y.; Ummadisingu, A.; Zakeeruddin, S. M.; Correa-Baena, J. P.; Tress, W. R.; Abate, A.; Hagfeldt, A.; Grätzel, M. Incorporation of Rubidium Cations into Perovskite Solar Cells Improves Photovoltaic Performance. *Science* **2016**, *354*, 206–209.
- (13) Saliba, M.; Matsui, T.; Seo, J. Y.; Domanski, K.; Correa-Baena, J. P.; Nazeeruddin, M. K.; Zakeeruddin, S. M.; Tress, W.; Abate, A.; Hagfeldt, A.; Grätzel, M. Cesium-Containing Triple Cation Perovskite Solar Cells: Improved Stability, Reproducibility and High Efficiency. *Energy Environ. Sci.* **2016**, *9*, 1989–1997.
- (14) Gao, X. X.; Xue, D. J.; Gao, D.; Han, Q.; Ge, Q. Q.; Ma, J. Y.; Ding, J.; Zhang, W.; Zhang, B.; Feng, Y.; Yu, G.; Hu, J. S. High-Mobility Hydrophobic Conjugated Polymer as Effective Interlayer for Air-Stable Efficient Perovskite Solar Cells. *Sol. RRL* **2019**, *3*, No. 1800232.
- (15) Jiang, Q.; Zhao, Y.; Zhang, X.; Yang, X.; Chen, Y.; Chu, Z.; Ye, Q.; Li, X.; Yin, Z.; You, J. Surface Passivation of Perovskite Film for Efficient Solar Cells. *Nat. Photonics* **2019**, *13*, 460–466.
- (16) Cheacharoen, R.; Rolston, N.; Harwood, D.; Bush, K. A.; Dauskardt, R. H.; McGehee, M. D. Design and Understanding of Encapsulated Perovskite Solar Cells to Withstand Temperature Cycling. *Energy Environ. Sci.* **2018**, *11*, 144–150.
- (17) Dong, D.; Li, J.; Cui, M.; Wang, J.; Zhou, Y.; Luo, L.; Wei, Y.; Ye, L.; Sun, H.; Yao, F. In Situ “Clickable” Zwitterionic Starch-Based Hydrogel for 3D Cell Encapsulation. *ACS Appl. Mater. Interfaces* **2016**, *8*, 4442–4455.

- (18) Acik, M.; Darling, S. B. Graphene in Perovskite Solar Cells: Device Design, Characterization and Implementation. *J. Mater. Chem. A* **2016**, *4*, 6185–6235.
- (19) Li, B.; Wang, M.; Subair, R.; Cao, G.; Tian, J. Significant Stability Enhancement of Perovskite Solar Cells by Facile Adhesive Encapsulation. *J. Phys. Chem. C* **2018**, *122*, 25260–25267.
- (20) Matteocci, F.; Cinà, L.; Lamanna, E.; Cacovich, S.; Divitini, G.; Midgley, P. A.; Ducati, C.; Di Carlo, A. Encapsulation for Long-Term Stability Enhancement of Perovskite Solar Cells. *Nano Energy* **2016**, *30*, 162–172.
- (21) Khenkin, M. V.; Katz, E. A.; Abate, A.; Bardizza, G.; Berry, J. J.; Brabec, C.; Brunetti, F.; Bulović, V.; Burlingame, Q.; Di Carlo, A.; Cheacharoen, R.; Cheng, Y. B.; Colmann, A.; Cros, S.; Domanski, K.; Dusz, M.; Fell, C. J.; Forrest, S. R.; Galagan, Y.; Di Girolamo, D.; Grätzel, M.; Hagfeldt, A.; von Hauff, E.; Hoppe, H.; Kettle, J.; Köbler, H.; Leite, M. S.; Liu, S.; Loo, Y. L.; Luther, J. M.; Ma, C. Q.; Madsen, M.; Manceau, M.; Matheron, M.; McGehee, M.; Meitzner, R.; Nazeeruddin, M. K.; Nogueira, A. F.; Odabaşı, Ç.; Osherov, A.; Park, N. G.; Reese, M. O.; De Rossi, F.; Saliba, M.; Schubert, U. S.; Snaith, H. J.; Stranks, S. D.; Tress, W.; Troshin, P. A.; Turkovic, V.; Veenstra, S.; Visoly-Fisher, I.; Walsh, A.; Watson, T.; Xie, H.; Yıldırım, R.; Zakeeruddin, S. M.; Zhu, K.; Lira-Cantu, M. Consensus Statement for Stability Assessment and Reporting for Perovskite Photovoltaics Based on ISOS Procedures. *Nat. Energy* **2020**, *5*, 35–49.
- (22) Nair, S.; Gohel, J. V. A Study on Optoelectronic Performance of Perovskite Solar Cell under Different Stress Testing Conditions. *Opt. Mater.* **2020**, *109*, No. 110377.
- (23) Shi, L.; Bucknall, M. P.; Young, T. L.; Zhang, M.; Hu, L.; Bing, J.; Lee, D. S.; Kim, J.; Wu, T.; Takamure, N.; McKenzie, D. R.; Huang, S.; Green, M. A.; Ho-Bailie, A. W. Y. Gas Chromatography-Mass Spectrometry Analyses of Encapsulated Stable Perovskite Solar Cells. *Science* **2020**, *368*, No. eaba2412.
- (24) Aranda, C.; Guerrero, A.; Bisquert, J. Crystalline Clear or Not: Beneficial and Harmful Effects of Water in Perovskite Solar Cells. *ChemPhysChem* **2019**, *20*, 2587–2599.
- (25) Aristidou, N.; Sanchez-Molina, I.; Chotchuangchuchaval, T.; Brown, M.; Martinez, L.; Rath, T.; Haque, S. A. The Role of Oxygen in the Degradation of Methylammonium Lead Trihalide Perovskite Photoactive Layers. *Angew. Chem., Int. Ed.* **2015**, *54*, 8208–8212.
- (26) Senocrate, A.; Acartürk, T.; Kim, G. Y.; Merkle, R.; Starke, U.; Grätzel, M.; Maier, J. Interaction of Oxygen with Halide Perovskites. *J. Mater. Chem. A* **2018**, *6*, 10847–10855.
- (27) Agroui, K.; Collins, G. Characterisation of EVA Encapsulant Material by Thermally Stimulated Current Technique. *Sol. Energy Mater. Sol. Cells* **2003**, *80*, 33–45.
- (28) Chen, B. M.; Peng, C. Y.; Cho, J. L.; Porter, G. A. Optimization of Solar Module Encapsulant Lamination by Optical Constant Determination of Ethylene-Vinyl Acetate. *Int. J. Photoenergy* **2015**, *2015*, No. 276404.
- (29) Lang, F.; Gluba, M. A.; Albrecht, S.; Rappich, J.; Korte, L.; Rech, B.; Nickel, N. H. Perovskite Solar Cells with Large-Area CVD-Graphene for Tandem Solar Cells. *J. Phys. Chem. Lett.* **2015**, *6*, 2745–2750.
- (30) Wang, R.; Xue, J.; Wang, K. L.; Wang, Z. K.; Luo, Y.; Fenning, D.; Xu, G.; Nuryyeva, S.; Huang, T.; Zhao, Y.; Yang, J. L.; Zhu, J.; Wang, M.; Tan, S.; Yavuz, I.; Houk, K. N.; Yang, Y. Constructive Molecular Configurations for Surface-Defect Passivation of Perovskite Photovoltaics. *Science* **2019**, *366*, 1509–1513.
- (31) Uddin, A.; Upama, M.; Yi, H.; Duan, L. Encapsulation of Organic and Perovskite Solar Cells: A Review. *Coatings* **2019**, *9*, No. 65.
- (32) Bunch, J. S.; Verbridge, S. S.; Alden, J. S.; Van Der Zande, A. M.; Parpia, J. M.; Craighead, H. G.; McEuen, P. L. Impermeable Atomic Membranes from Graphene Sheets. *Nano Lett.* **2008**, *8*, 2458–2462.
- (33) Sheehy, D. E.; Schmalian, J. Optical Transparency of Graphene as Determined by the Fine-Structure Constant. *Phys. Rev. B* **2009**, *80*, No. 193411.
- (34) Cheacharoen, R.; Boyd, C. C.; Burkhard, G. F.; Leijtens, T.; Raiford, J. A.; Bush, K. A.; Bent, S. F.; McGehee, M. D. Encapsulating Perovskite Solar Cells to Withstand Damp Heat and Thermal Cycling. *Sustainable Energy Fuels* **2018**, *2*, 2398–2406.
- (35) Cheacharoen, R.; Bush, K. A.; Rolston, N.; Harwood, D.; Dauskardt, R. H.; McGehee, M. D. In *Damp Heat, Temperature Cycling and UV Stress Testing of Encapsulated Perovskite Photovoltaic Cells*, 2018 IEEE 7th World Conference on Photovoltaic Energy Conversion (WCPEC) (A Joint Conference of 45th IEEE PVSC, 28th PVSEC & 34th EU PVSEC); IEEE, 2018; pp 3498–3502.
- (36) You, P.; Liu, Z.; Tai, Q.; Liu, S.; Yan, F. Efficient Semitransparent Perovskite Solar Cells with Graphene Electrodes. *Adv. Mater.* **2015**, *27*, 3632–3638.
- (37) Kim, G.-H.; Jang, H.; Yoon, Y. J.; Jeong, J.; Park, S. Y.; Walker, B.; Jeon, I.-Y.; Jo, Y.; Yoon, H.; Kim, M.; Baek, J.-B.; Kim, D. S.; Kim, J. Y. Fluorine Functionalized Graphene Nano Platelets for Highly Stable Inverted Perovskite Solar Cells. *Nano Lett.* **2017**, *17*, 6385–6390.
- (38) Li, H.; Tao, L.; Huang, F.; Sun, Q.; Zhao, X.; Han, J.; Shen, Y.; Wang, M. Enhancing Efficiency of Perovskite Solar Cells via Surface Passivation with Graphene Oxide Interlayer. *ACS Appl. Mater. Interfaces* **2017**, *9*, 38967–38976.
- (39) Yang, Q.-D.; Li, J.; Cheng, Y.; Li, H.-W.; Guan, Z.; Yu, B.; Tsang, S.-W. Graphene Oxide as an Efficient Hole-Transporting Material for High-Performance Perovskite Solar Cells with Enhanced Stability. *J. Mater. Chem. A* **2017**, *5*, 9852–9858.
- (40) Kim, J. M.; Kim, S.; Choi, S. H. High-Performance n-i-p-Type Perovskite Photodetectors Employing Graphene-Transparent Conductive Electrodes N-Type Doped with Amine Group Molecules. *ACS Sustainable Chem. Eng.* **2019**, *7*, 734–739.
- (41) Zhu, M.; Liu, W.; Ke, W.; Xie, L.; Dong, P.; Hao, F. Graphene-Modified Tin Dioxide for Efficient Planar Perovskite Solar Cells with Enhanced Electron Extraction and Reduced Hysteresis. *ACS Appl. Mater. Interfaces* **2019**, *11*, 666–673.
- (42) Kim, K.; Lee, Z.; Regan, W.; Kisielowski, C.; Crommie, M. F.; Zettl, A. Grain Boundary Mapping in Polycrystalline Graphene. *ACS Nano* **2011**, *5*, 2142–2146.
- (43) Kim, H. W.; Yoon, H. W.; Yoon, S.; Yoo, B. M.; Ahn, B. K.; Cho, Y. H.; Shin, H. J.; Yang, H.; Paik, U.; Kwon, S. Selective Gas Transport Through Few-Layered Graphene and Graphene Oxide Membranes. *Science* **2013**, *342*, 91–95.
- (44) You, P.; Liu, Z.; Tai, Q.; Liu, S.; Yan, F. Efficient Semitransparent Perovskite Solar Cells with Graphene Electrodes. *Adv. Mater.* **2015**, *27*, 3632–3638.
- (45) Chen, Y.; Yue, Y.; Wang, S.; Zhang, N.; Feng, J.; Sun, H. Graphene as a Transparent and Conductive Electrode for Organic Optoelectronic Devices. *Adv. Electron. Mater.* **2019**, *5*, No. 1900247.
- (46) Tang, X.; Brandl, M.; May, B.; Levchuk, I.; Hou, Y.; Richter, M.; Chen, H.; Chen, S.; Kahmann, S.; Osvet, A.; Maier, F.; Steinrück, H. P.; Hock, R.; Matt, G. J.; Brabec, C. J. Photoinduced Degradation of Methylammonium Lead Triiodide Perovskite Semiconductors. *J. Mater. Chem. A* **2016**, *4*, 15896–15903.
- (47) Zhang, X.; Li, Z.; Ding, Y.; Hu, L.; Ye, J.; Pan, X.; Dai, S. Highly Efficient and Stable Perovskite Solar Cell Prepared from an: In Situ Pre-Wetted PbI₂ Nano-Sheet Array Film. *Sustainable Energy Fuels* **2017**, *1*, 1056–1064.
- (48) Stoumpos, C. C.; Malliakas, C. D.; Kanatzidis, M. G. Semiconducting Tin and Lead Iodide Perovskites with Organic Cations: Phase Transitions, High Mobilities, and near-Infrared Photoluminescent Properties. *Inorg. Chem.* **2013**, *52*, 9019–9038.
- (49) Han, G. H.; Güneş, F.; Bae, J. J.; Kim, E. S.; Chae, S. J.; Shin, H. J.; Choi, J. Y.; Pribat, D.; Lee, Y. H. Influence of Copper Morphology in Forming Nucleation Seeds for Graphene Growth. *Nano Lett.* **2011**, *11*, 4144–4148.
- (50) Zhao, L.; Tian, H.; Silver, S. H.; Kahn, A.; Ren, T. L.; Rand, B. P. Ultrasensitive Heterojunctions of Graphene and 2D Perovskites Reveal Spontaneous Iodide Loss. *Joule* **2018**, *2*, 2133–2144.
- (51) Hoke, E. T.; Slotcavage, D. J.; Dohner, E. R.; Bowring, A. R.; Karunadasa, H. I.; McGehee, M. D. Reversible Photo-Induced Trap

Formation in Mixed-Halide Hybrid Perovskites for Photovoltaics. *Chem. Sci.* **2015**, *6*, 613–617.

(52) Lee, J. W.; Kim, D. H.; Kim, H. S.; Seo, S. W.; Cho, S. M.; Park, N. G. Formamidinium and Cesium Hybridization for Photo- and Moisture-Stable Perovskite Solar Cell. *Adv. Energy Mater.* **2015**, *5*, No. 1501310.

(53) Calizo, I.; Bejenari, I.; Rahman, M.; Liu, G.; Balandin, A. A. Ultraviolet Raman Microscopy of Single and Multilayer Graphene. *J. Appl. Phys.* **2009**, *106*, No. 043509.

(54) Brownson, D. A. C.; Banks, C. E. CVD Graphene Electrochemistry: The Role of Graphitic Islands. *Phys. Chem. Chem. Phys.* **2011**, *13*, 15825–15828.

(55) Kasap, S.; Khaksaran, H.; Çelik, S.; Özkaya, H.; Yanik, C.; Kaya, I. I. Controlled Growth of Large Area Multilayer Graphene on Copper by Chemical Vapour Deposition. *Phys. Chem. Chem. Phys.* **2015**, *17*, 23081–23087.

(56) Yoon, T.; Mun, J. H.; Cho, B. J.; Kim, T. S. Penetration and Lateral Diffusion Characteristics of Polycrystalline Graphene Barriers. *Nanoscale* **2014**, *6*, 151–156.

(57) Huang, P. Y.; Ruiz-Vargas, C. S.; Van Der Zande, A. M.; Whitney, W. S.; Levendorf, M. P.; Kevek, J. W.; Garg, S.; Alden, J. S.; Hustedt, C. J.; Zhu, Y.; Park, J.; McEuen, P. L.; Muller, D. A. Grains and Grain Boundaries in Single-Layer Graphene Atomic Patchwork Quilts. *Nature* **2011**, *469*, 389–392.

(58) Grantab, R.; Shenoy, V. B.; Ruoff, R. S. Anomalous Strength Characteristics of Tilt Grain Boundaries in Graphene. *Science* **2010**, *330*, 946–948.

(59) Duong, D. L.; Han, G. H.; Lee, S. M.; Gunes, F.; Kim, E. S.; Kim, S. T.; Kim, H.; Ta, Q. H.; So, K. P.; Yoon, S. J.; Chae, S. J.; Jo, Y. W.; Park, M. H.; Chae, S. H.; Lim, S. C.; Choi, J. Y.; Lee, Y. H. Probing Graphene Grain Boundaries with Optical Microscopy. *Nature* **2012**, *490*, 235–239.

(60) Shahriary, L.; Athawale, A. A. Graphene Oxide Synthesized by Using Modified Hummers Approach. *Int. J. Renewable Energy Environ. Eng.* **2014**, *2*, 58–63.

(61) Tzeng, P.; Stevens, B.; Devlaming, I.; Grunlan, J. C. Polymer-Graphene Oxide Quadlayer Thin-Film Assemblies with Improved Gas Barrier. *Langmuir* **2015**, *31*, 5919–5927.

(62) Liu, H.; Meng, J.; Zhang, X.; Chen, Y.; Yin, Z.; Wang, D.; Wang, Y.; You, J.; Gao, M.; Jin, P. High-Performance Deep Ultraviolet Photodetectors Based on Few-Layer Hexagonal Boron Nitride. *Nanoscale* **2018**, *10*, 5559–5565.

(63) Ramírez, J.; Urbina, A. D.; Kleinschmidt, A. T.; Finn, M.; Edmunds, S. J.; Esparza, G. L.; Lipomi, D. J. Exploring the Limits of Sensitivity for Strain Gauges of Graphene and Hexagonal Boron Nitride Decorated with Metallic Nanoislands. *Nanoscale* **2020**, *12*, 11209–11221.